A version of this chapter has been published in Phys Med Biol, vol. 51, pp. 6061-75, 2006.

"There's a way to do it better – find it"
Thomas A. Edison

Chapter 4. Micro-CT Lung Imaging

Abstract: Micro-Computed Tomography (micro-CT) is becoming increasingly utilized for high-resolution non-invasive fast throughput small animal imaging. Because of the inherent sensitivities in acquiring perfectly aligned projection data as well as the loss through the reconstruction process, micro-CT systems do not always live up to advertised specifications. Respiratory research of mice using small animal imaging systems such as micro-CT have also been further hindered by the limited resolution and Signal to Noise Ratio (SNR) as a result of respiratory motion artifacts.

In the first section of this chapter, we present several techniques developed and implemented to reduce commonly associated artifacts and increase the resolution and contrast of micro-CT images. In the second section of this chapter, we present a novel breath hold technique for capturing the lung microstructure *in vivo* using micro-CT. We have termed this new technique Intermittent Iso-pressure Breath Hold (IIBH) gating, which essentially pauses the respiratory motion during image acquisition, increasing the resolution and SNR of the reconstructed images. We compare four gating techniques, i.e. no gating, Late Expiratory (LE) gating, Late Inspiratory (LI) gating and finally Intermittent Iso-pressure Breath Hold (IIBH) gating. Quantitatively, we compare several common image analysis methods used to extract valuable physiologic and anatomic metrics, and show that the IIBH technique produces the most representative and repeatable results.

4.1 Introduction

Advances in our understanding of the interrelatedness of the pulmonary structure and function between animals and humans have recently been accelerated through the use of non-invasive imaging modalities such as Multi-Detector Computed Tomography (MDCT) [143-145]. Complexities in developing mouse models of human diseases have been dramatically facilitated by the recent completion of the

Mouse Genome Project [1, 2] and associated mouse model research [3-7]. There are now many mouse models of pulmonary disease and the relevance to and utility of these has been previously published [6, 88].

Micro-Computed Tomography (micro-CT) is an X-ray modality, which has become increasingly available as a solution to high-resolution non-invasive fast through-put small animal imaging [39]. Theoretically, through calculation of focal spot size, detector pitch and other geometric variables [39], commercial micro-CT systems for use on live animals have been quoted with resolving powers down to 9 microns [40]. Because of the inherent sensitivities of acquiring perfectly aligned projection data as well as the loss through the reconstruction process, the resolution of the final image is always lower. This procedure of acquiring data for filtered back projection reconstruction requires not only very accurate alignment of the gantry or point at which the projection angle is rotated, but also requires that the object be completely still during acquisition.

In the following chapter, we describe techniques for reducing the image resolution and quality artifacts associated with high-resolution micro-CT imaging and implement a novel breath hold imaging technique for acquiring high-resolution imaging of the lung *in vivo*.

4.2 Micro-CT Artifact Reduction and Image Processing

4.2.1 Introduction

Computed tomography, including clinical and pre-clinical micro-CT systems, was initially introduced as a qualitative imaging modality. Each manufacturer performs image quality measures using proprietary measures; the United States-FDA or Australian-TGA do not have compliance requirements for image quality. This is a problem when using CT data sets for quantitative measures because even repeatability within the same scanner is uncertain. Not surprisingly, this problem is more prominent in pre-clinical micro-CT systems where, in many cases, hardware specifications are not always met, let alone image quality and repeatability specifications. In order to perform accurate quantitative measurements using micro-CT systems in research, a deep understanding of the physics and the computer related algorithms is required. This knowledge provides the user with the ability to correlate what a pixel or voxel actually represents, and what information can be ascertained for such datasets.

Some common problems related to micro-CT imaging that should be addressed prior to quantification include: accurate scanner geometry calibration, calibration of the detector in dark and bright fields, beam hardening calibration, water phantom calibration and minimizing aliasing due to insufficient sampling or number of acquired projections. Such problems lead to many artifacts seen in reconstructed CT images including, but not limited to: ring artifacts, beam hardening artifacts, incorrect Hounsfield scaling, wind swept images (center offset misalignment) and ghosted images (source-to-object distance rotational misalignment).

In this thesis, several practical approaches have been taken to reduce such artifacts and problems associated with research level pre-clinical micro-CT systems. These include pre-conditioning the X-ray source prior to scanning and maintaining temperatures within the micro-CT enclosure and room at a constant level in order to reduce changes in the detector sensitivity due to thermal variations. Implementation of a pre-reconstruction processing step further reduces the effects of detector element insensitivities, which frequently result in ring artifacts. Additionally, accurate calibration of the scanner geometry using a custom developed phantom and computer algorithm to reduce both center offset misalignment and source to detector misalignment during acquisition, has been developed and implemented. Finally, a practical technique for reducing the effects of beam hardening as a result of the polychromatic X-ray source using a custom phantom and non-linear polynomial correction is implemented.

Although it is difficult to produce a perfectly reconstructed data set, inhomogeneity within and across datasets can be reduced through a sequence of well thought out practical measures.

4.2.2 Methods and Materials

4.2.2.1 Imtek Micro-CAT II Scanner

A Micro CAT II (Siemens Pre-Clinical, Knoxville, Tennessee) micro-computed tomography scanner, shown in Figure 4.1, was used throughout this study. This system was fitted with a Kevex (Thermo Electron Corp., Waltham, Massachusetts) micro-focus X-ray source capable of 0-500 μA and 0-130 kVp with a maximum total power output of 65 Watts.

Figure 4.1: Siemens MicroCAT-II micro-Computed Tomography scanner.

4.2.2.2 Dynamic Source to Detector Correction

The Siemens MicroCAT II incorporates a stationary specimen stage and a rotating source and detector couple; imperfections in the gantry in addition to gravitational forces result in source-to-object-to-detector distance variations. If this wobble or variation creates a shift greater than the resolving pixel dimension of the system, this results in ghosting of the reconstructed images. Since the pixel dimensions of this system are quite small, i.e. in the order of 10-100 microns, small variations in the gantry will cause visible artifacts in the reconstructed images. The reconstruction algorithm can, however, be modified to take into account the change in source-to-object and object-to-detector distances for each projection. We have developed a relatively simple technique for determining this shift and incorporating the dynamic source to object and object to detector distances into the reconstruction algorithm.

First, a phantom was built incorporating a 12.7mm brass ball bearing embedded within a polyurethane foam cylinder as shown in Figure 4.2. The phantom was then scanned over 360 degrees. The projection images are processed using an implementation of the Otsu thresh-holding technique [146] and morphological operators in order to determine the area of the ball bearing at each projection angle. The area information was converted into a translational shift, and hence a source-to-object and object-to-detector distance was calculated for each projection/angle of view.

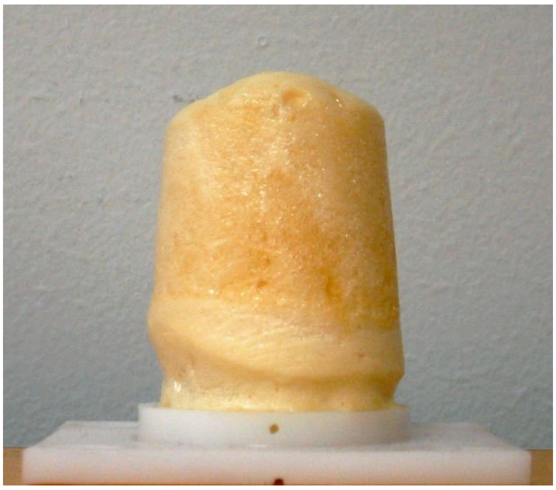

Figure 4.2: Brass ball bearing phantom encased in polyurethane foam.

The conversion between the area of the ball bearing in the projection and the shift in translation along the source-to-detector ray was calculated using a prior calibration step. This calibration step includes acquiring projection images of the ball bearing phantom at varying source-to-object and object-to-detector distances. The change in step distance between each ball projection and the pixel pitch of the detector were known. From this information the source-to-object and object-to-detector could be calculated using the geometric concept of similar triangles. Figure 4.3 represents an illustration of the geometry of the ball phantom at two distances.

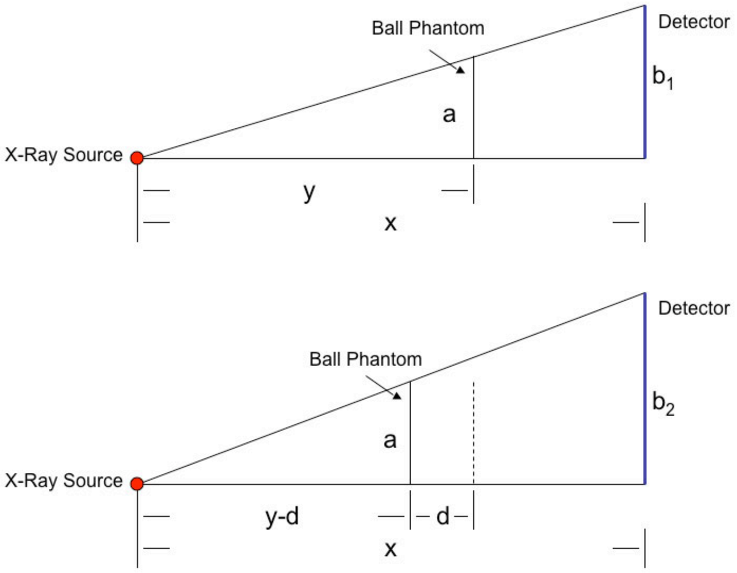

Figure 4.3: Schematic geometric illustration for calculating the source-to-object and source-to-detector distance using the ball bearing phantom X-ray projections at two known distances.

Utilizing the concept of similar triangles, we have two equations and two unknowns for each geometry as represented in equations 4.1-4.2 and 4.3-4.4, respectively.

$$x = \frac{b_1 y}{a} \tag{4.1}$$

$$y = \frac{ax}{b_1} \tag{4.2}$$

$$x = \frac{b_2(y-d)}{a} \tag{4.3}$$

$$y = \frac{ax + b_2 d}{b_2} \tag{4.4}$$

Through simultaneous equations we can calculate a unique solution for the source-to-object (y) and source-to-detector (x) distance as shown in equation 4.5 & 4.6.

$$y = \frac{b_2 d}{b_2 - b_1} \tag{4.5}$$

$$x = \frac{\frac{b_1 b_2 d}{b_2 - b_1}}{a} \tag{4.6}$$

An example of the ball bearing phantom X-ray projections at two known separation distances is shown in Figure 4.4.

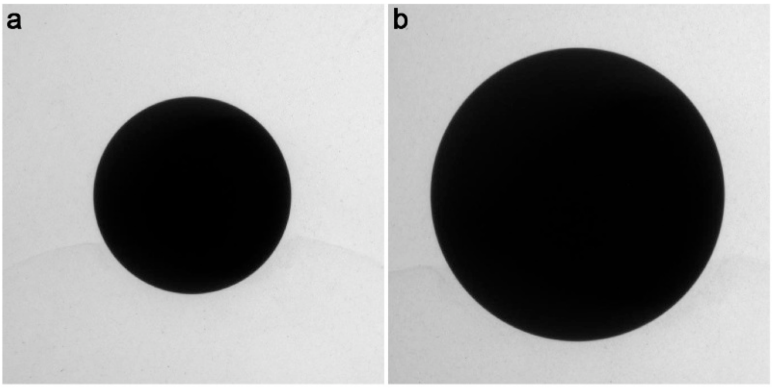

Figure 4.4: Ball phantom projection, a) position 1 – closer to detector, b) position 2 – closer to source.

Figure 4.5 represents a plot of the change in ball bearing diameter (calculated indirectly through the area of a circle) as seen by the detector over 360 degrees.

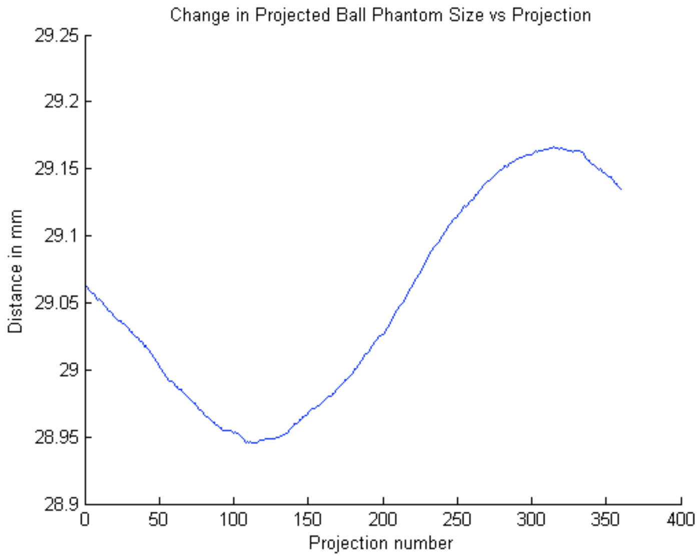

Figure 4.5: Change in projected ball phantom diameter in mm (y-axis) over 360 degrees (x-axis).

Using the calculated ball bearing area for each projection over 360 degrees, the change in distance of the object position can be calculated using a prior relationship between the area of the ball bearing phantom versus the real translated distance as shown in Figure 4.6.

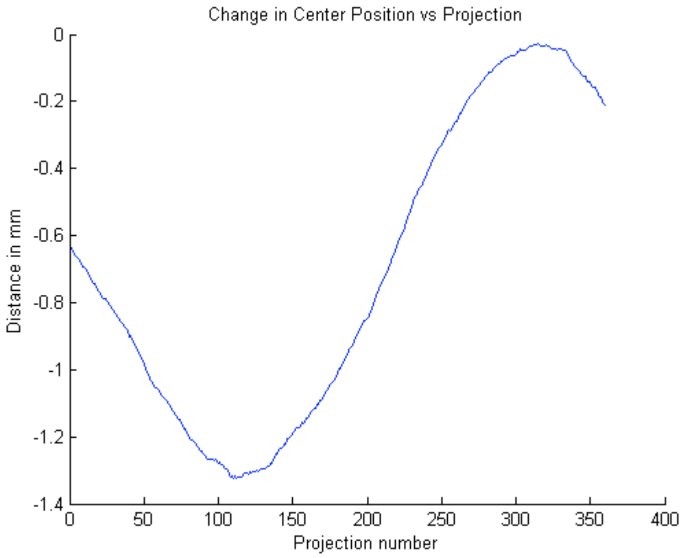

Figure 4.6: Calculated change in object position with respect to source and detector in mm (y-axis) over 360 degrees (x-axis).

The area of the ball bearing was determined for each projection directly from the image; the theoretical radius was then calculated using πr^2, rather than measuring the radius directly from the image. This approach was taken since the accuracy of determining the projected ball bearing area from the image was significantly greater as there are many more pixels representing the area versus a straight-line of pixels measuring the diameter.

4.2.2.3 Dynamic Center Offset Correction

Using the ball bearing phantom and a similar image analysis approach as described above, we can calculate the change in center offset of the object over the projection angles. Here, the center of the ball bearing phantom is calculated using a center weighted algorithm after binary segmentation, and its shift from the center of the detector array is determined for every projection angle in a custom Matlab (Mathworks, Natick MA) program. The dynamic center offset values calculated here can then be incorporated into the Cobra reconstruction algorithm (EXXIM Computing Corp, California) to offset errors introduced by the gantry shift.

4.2.2.4 Pre-reconstruction Ring Artifact Correction

The insensitivities between detector elements are normally well calibrated through the acquisition of a series of dark and bright field images prior to scanning of the specimen. Here, a number of images are acquired with no X-ray energy (dark field) and another number of images with the X-ray energy at maximum (bright-field). The average for each is then used as an offset for subsequent projections acquired from the specimen. Since this calibration step is performed at the beginning of a CT scan prior to scanning the specimen, there are slight changes to the detector elements over the span of the specimen scan. In order to better offset each projection with a dark and bright field image, they must be acquired prior to each specimen projection, which is practically not feasible. In this thesis, we perform ring artifact reduction processing on each sinogram within a dataset in order to reduce the effects of the insensitivities from detector elements during the reconstruction phase. Since the sinogram represents the same detector row over the number of projection angles, insensitivities in any detector element result in vertical lines in the sinogram as shown in Figure 4.7 (a). Here, we calculate the average intensity profile across each row in the sinogram. We then perform a low pass filter on this intensity profile and subtract it from the original intensity profile. The resultant difference profile is subsequently subtracted from every row in the sinogram in order to reduce spikes representing the line artifacts while maintaining true intensity changes due to the object of interest. Figure 4.7 (b) represents an example of an average intensity profile (red), smoothed intensity profile (black) and finally the resultant difference profile (blue). The difference profile has been magnified for illustration purposes. A magnified region from Figure 4.7 (c) and (d) is shown in Figure 4.8 to better illustrate the smoothing filter.

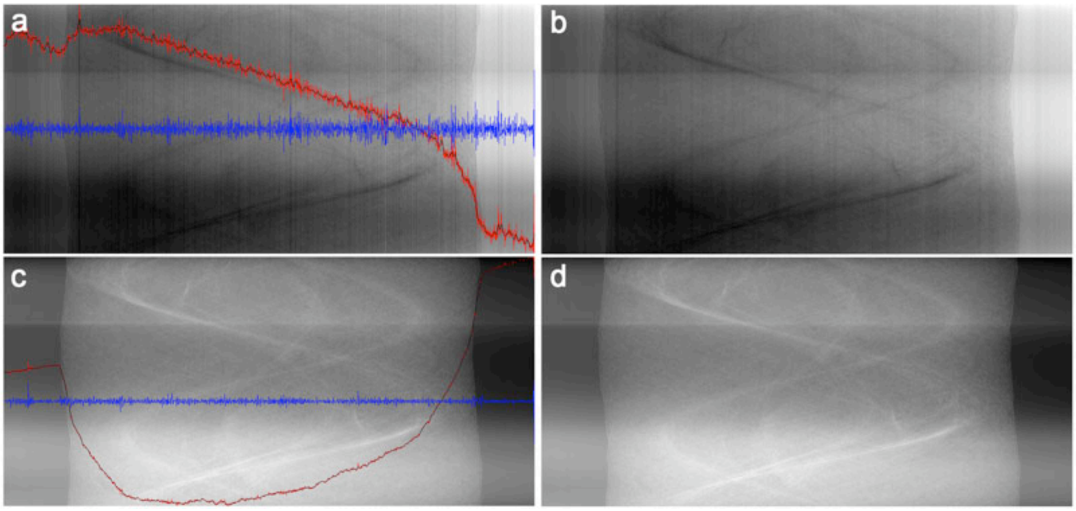

Figure 4.7: a) original sinogram with average column intensity profile (red), smoothed profile (black) and difference between the normal and smoothed profile (blue), b) original sinogram with filter applied c) calibrated sinogram with average column intensity profile (red), smoothed profile (black) and difference between the normal and smoothed profile (blue), d) calibrated sinogram with filter applied.

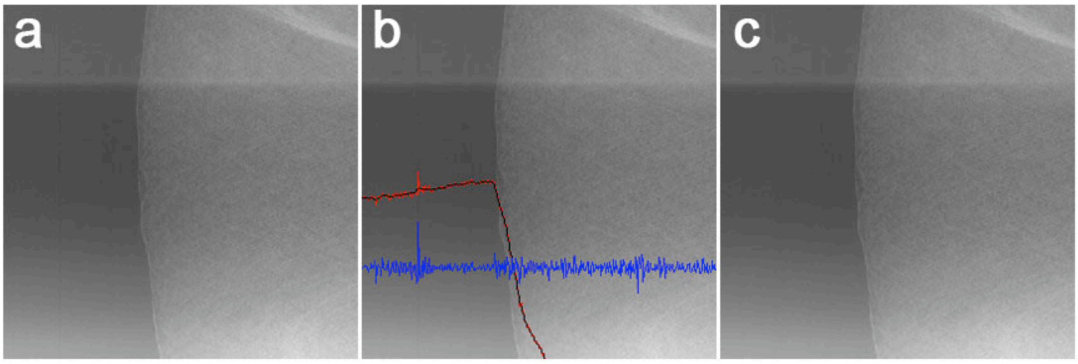

Figure 4.8: Magnified sinogram, a) original sinogram, b) original sinogram with average column intensity profile (red), smoothed profile (black) and difference between the normal and smoothed profile (blue), b) original sinogram with filter applied.

4.2.2.5 Beam Hardening Correction

As a result of the polychromatic X-ray source, the degree to which X-ray photons are absorbed by the specimen is not only dependent on the X-ray energy or wavelength, but also the thickness of the object. For thin specimens, this is not a major concern, but in small animal imaging this is a major problem and results in a varying radio-density across the reconstructed image. Figure 4.9 represents a tomographic reconstructed water phantom scan. Here we can see the clear in-homogeneity of the density values across the phantom.

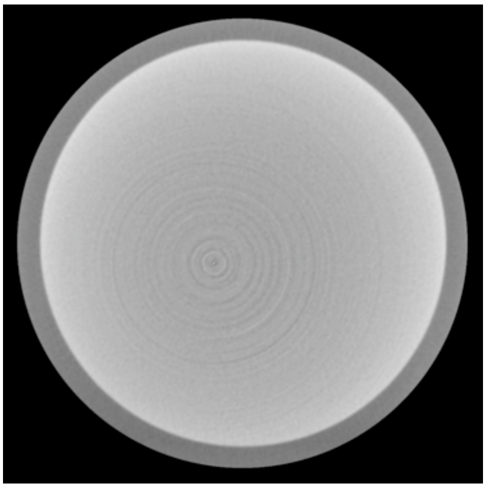

Figure 4.9: Water phantom scan with no hardware filter.

In X-ray imaging the most common technique used for reducing beam hardening artifacts seen in Figure 4.9 is placing a ‘hardware’ filter in front of the X-ray source. The hardware filter, which is commonly a thin metal plate, reduces the low energy photons that are the predominant cause of this cupping artifact. Using a 3mm Aluminum filter, the example in Figure 4.9 has been re-scanned and reconstructed as shown in Figure 4.10, here we can see a clear reduction in the cupping beam hardening artifact.

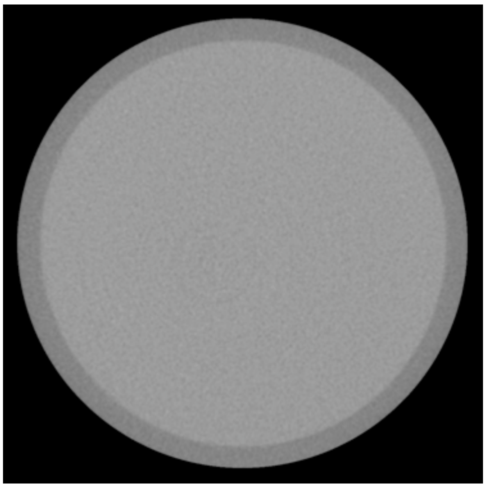

Figure 4.10: Water phantom scan with 3mm Aluminum filter.

In addition to hardware filtering, there are also several computational techniques that have been previously introduced to reduce beam-hardening artifacts [147-154]. The simplest is a widely implemented a priori, non-linear polynomial correction, which does not pose a heavy computational burden [150]. This technique uses prior information about the attenuation versus thickness of the same object at the same X-ray energy to model the beam hardening effect.

The Cobra (EXXIM Computing Corp, California) reconstruction algorithm allows this simple polynomial correction when pre-determined coefficients are given. In order to calculate the coefficients, a phantom was made consisting of a water equivalent plastic machined with three diameter cylinders in a pyramid fashion. Figure 4.11 (a) represents the custom made phantom and Figure 4.11 (b) the projection X-ray. Using this phantom, we can perform a single CT scan for every scanner setting and fit a third order polynomial to the change in density across the phantom at each thickness ***t***.

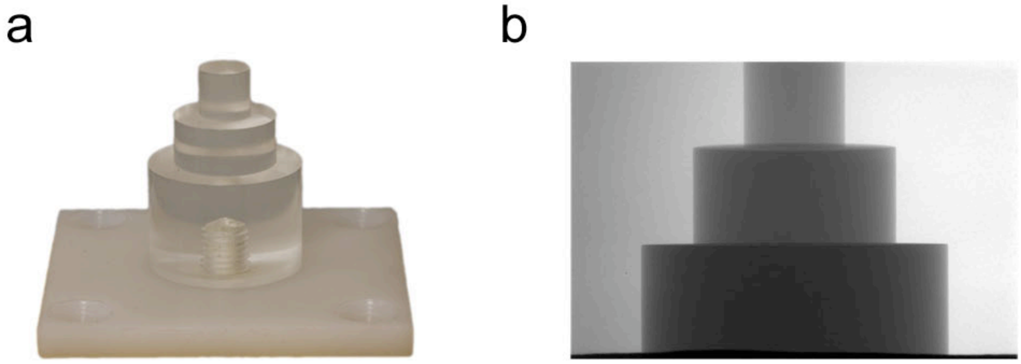

Figure 4.11: (a) Beam hardening correction phantom and (b) representative projection X-ray image.

To calculate the polynomial coefficients, we first performed a micro-CT scan at the desired scan settings. A projection X-ray and attenuation profile plot across the phantom is shown in Figure 4.12 (a-b).

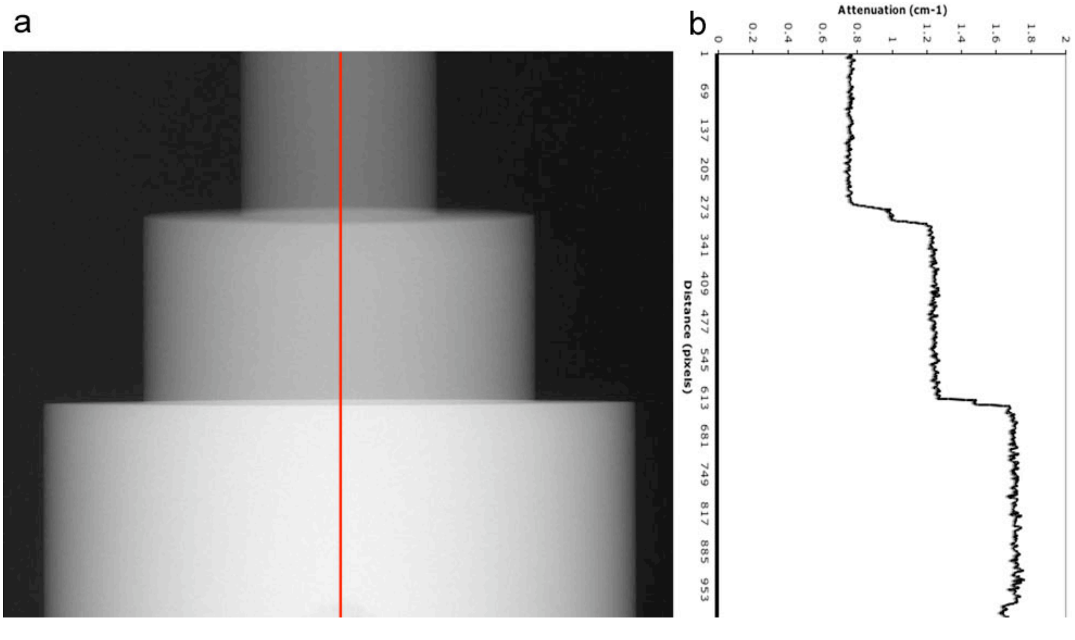

Figure 4.12: (a) log calibrated projection X-ray of the water phantom with 0.5mm Al filter, (b) attenuation profile plot across the varying thickness material as depicted in the red line in (a).

The projection X-ray has been log calibrated against the dark-field and bright-field images acquired at the beginning of the scan using equation 4.7

$$S(u,v) = \log(S_{\text{Bright}}(u,v) - S_{\text{Dark}}(u,v)) - \log(S_{\text{Projection}}(u,v) - S_{\text{Dark}}(u,v)), \qquad 4.7$$

where S_{Bright} is the bright-field calibration image, S_{Dark} is the dark-field calibration image and $S_{\text{Projection}}$ is the input projection containing the object of interest. The output S is represented in attenuation values cm^{-1}.

From the resultant projection image S, we obtain the thickness versus attenuation values of the water phantom at the current X-ray settings. We then fit a third order polynomial forced to cross the origin with the form shown in equation 4.8. The coefficients of this polynomial are then used in combination with the EXXIM Cobra (EXXIM Computing Corp., California) reconstruction algorithm to correct for the beam hardening.

$$S_{\text{output}} = a_0 + a_1 S_{\text{input}} + a_2 S_{\text{input}}^2 + a_3 S_{\text{input}}^3 , \qquad 4.8$$

where S_{input} is the logged calibrated signal attenuation value, a_n are the coefficients for the polynomial correction, and a_0 is set to zero.

4.2.3 Results

4.2.3.1 Dynamic Source to Detector Correction

An example of the resultant reconstructed image using the dynamic source to object and object to detector values calculated using the techniques outlined in Section 4.2.2.2, is shown in Figure 4.13. In Figure 4.13 (a) we can clearly see the characteristic shadowing effect of a mis-calibrated system. When corrected as shown in Figure 4.13 (b), the definition of the edges is significantly improved and much of the ghosting seen in Figure 4.13 (a) has been eliminated.

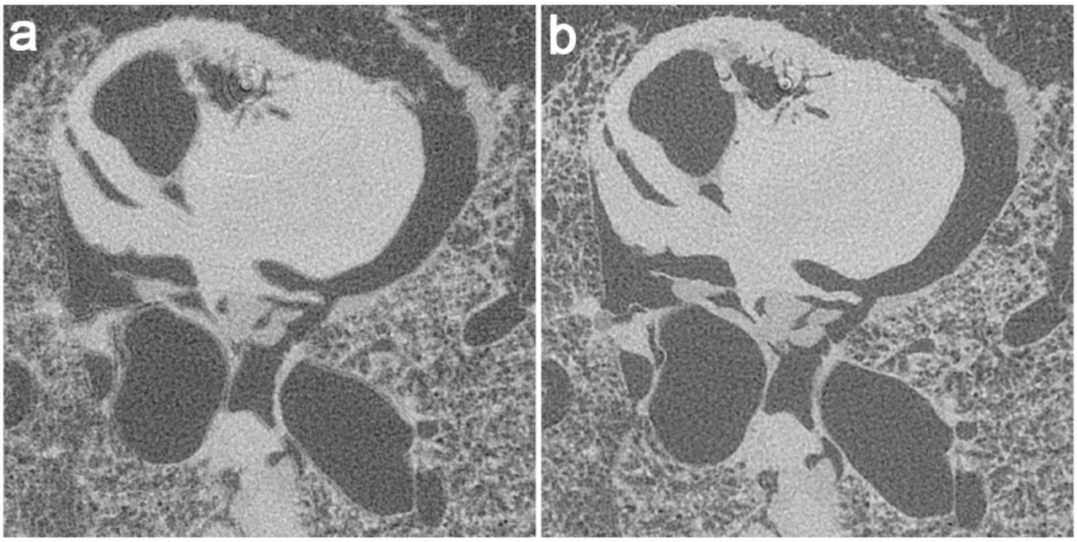

Figure 4.13: Ex vivo lung axial slice, a) normal reconstruction, b) reconstruction with dynamic source to detector distance.

4.2.3.2 Dynamic Center Offset Correction

The dynamic center offset correction detailed in Section 4.2.2.3 has been implemented on the original dataset used in the example above; Figure 4.14 (a) represents the original axial slice and Figure 4.14 (b) the center offset corrected axial slice. Again, we can see an improvement in the corrected image, although not as dramatic as the dynamic source detector correction illustrated above.

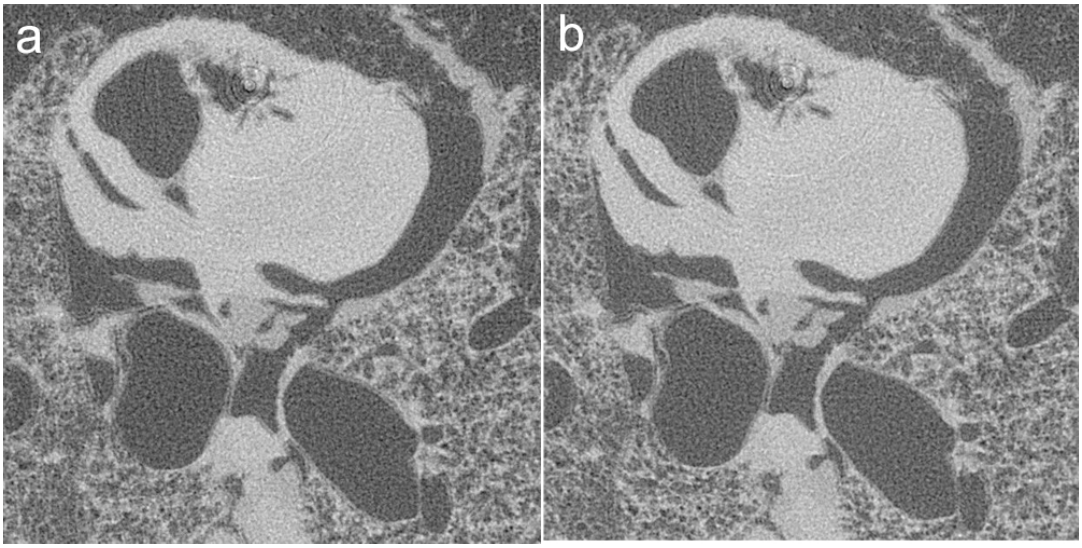

Figure 4.14: Ex vivo fixed lung axial slice, (a) normal reconstruction, (b) reconstruction with dynamic center offset distance.

4.2.3.3 Pre-reconstruction Ring Artifact Correction

An example of an *in vivo* mouse lung axial slice with severe and moderate ring artifacts is shown in Figure 4.15 (a) & (c), respectively. Although ring artifacts with greater severity than that shown in Figure 4.15 (a) are possible, with the appropriate precaution such as pre-conditioning the X-ray tube prior to imaging, ring artifacts should not exceed that seen in Figure 4.15 (c).

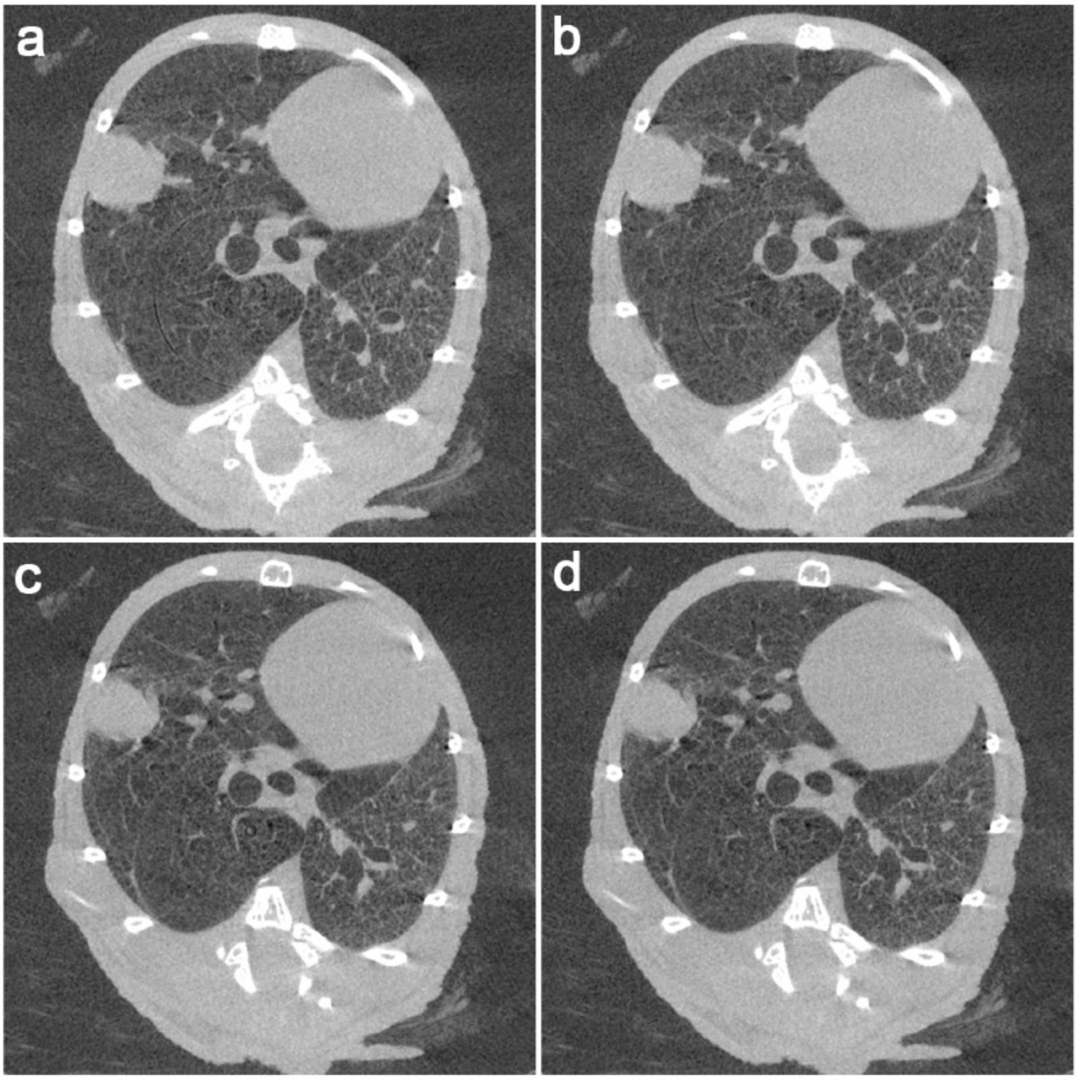

Figure 4.15: a) Original axial lung image with moderately severe ring artifacts, b) image a) post ring artifact reduction, c) Original axial lung image with moderate ring artifacts, d) image c) post ring artifact reduction.

4.2.3.4 Beam Hardening Correction

A reconstructed axial slice for each segment of the beam hardening phantom, corresponding to 1, 2 & 3cm of thickness, is shown in Figure 4.16 (a-c), respectively.

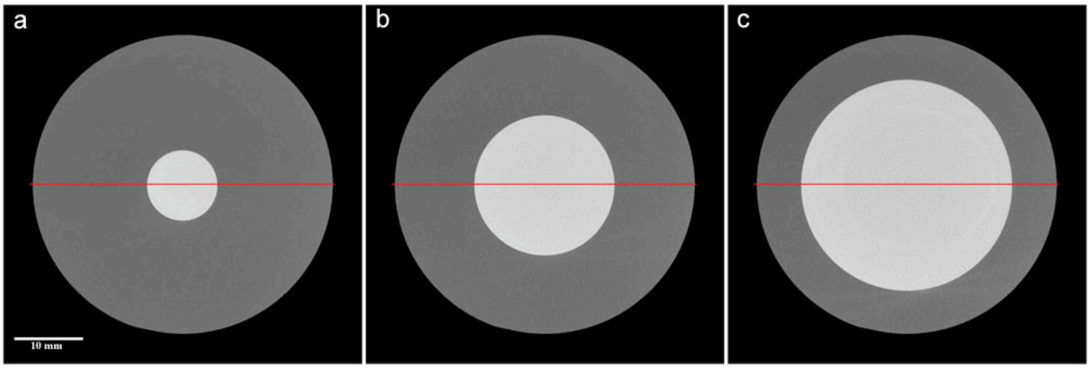

Figure 4.16: Beam hardening water phantom, (a) 1 cm phantom axial slice, (b) 2 cm phantom axial slice and (c) 3 cm phantom axial slice, red line shown for location of profile plots in Figure 4.17.

Figure 4.17 illustrates three profile plots for each red line represented in Figure 4.16 (a-c). Here, we can see the cupping artifact for each thickness, but also the difference in the attenuation values versus thickness for a non-corrected reconstruction.

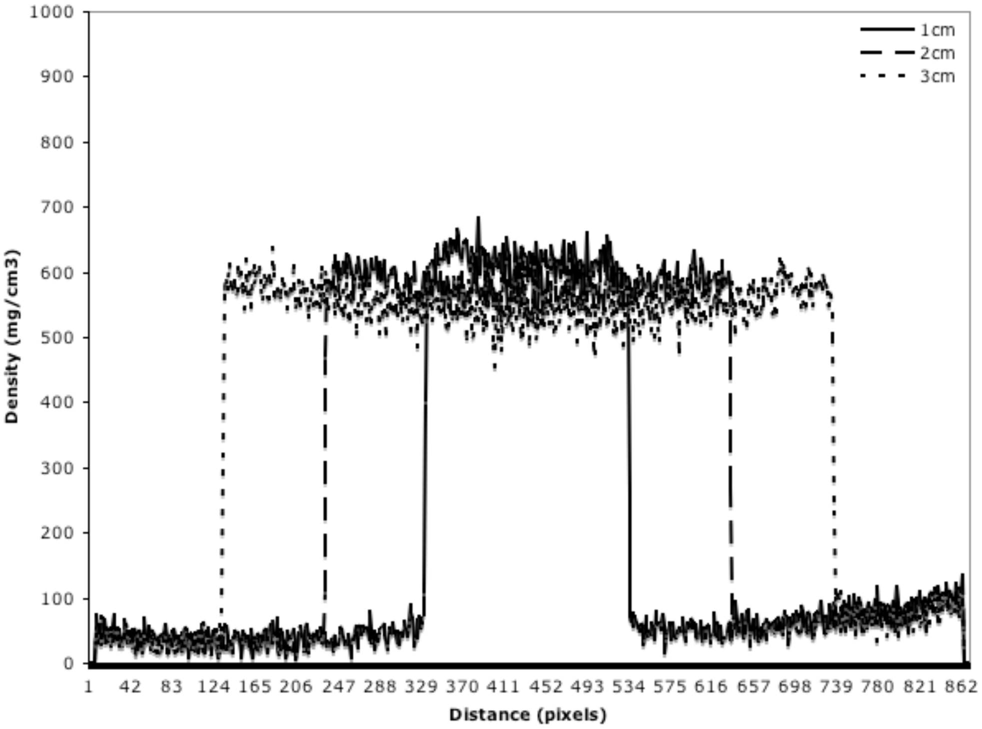

Figure 4.17: Profile plot across red line shown in Figure 4.16 (a-c) for water phantom at 1, 2 & 3cm thickness.

A polynomial corrected reconstruction for the water beam hardening phantom corresponding to 1, 2 & 3cm of thickness is shown in Figure 4.18 (a-c), respectively.

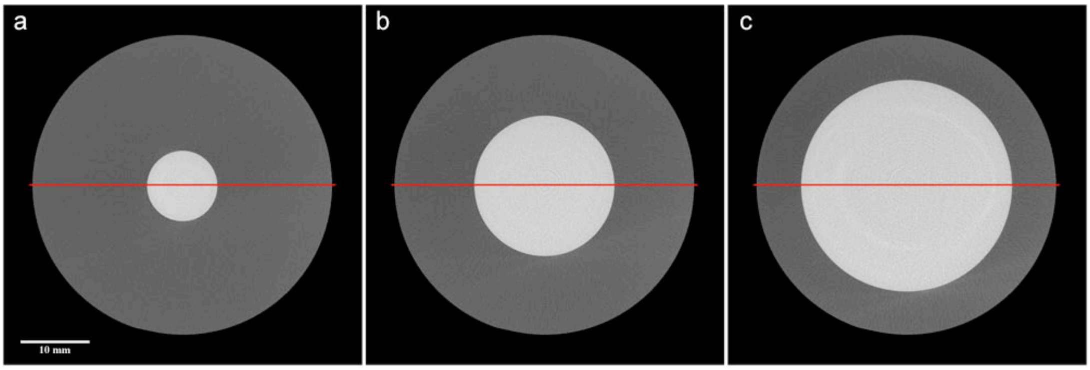

Figure 4.18: Corrected beam hardening water phantom, (a) 1 cm phantom axial slice, (b) 2 cm phantom axial slice and (c) 3 cm phantom axial slice, red line shown for location of profile plots in Figure 4.19.

Figure 4.19 illustrates the profile plot for each red line represented in Figure 4.18 (a-c). Here, we can see the corrective effect of implementing the polynomial correction on the attenuation values of the phantom at the different thicknesses.

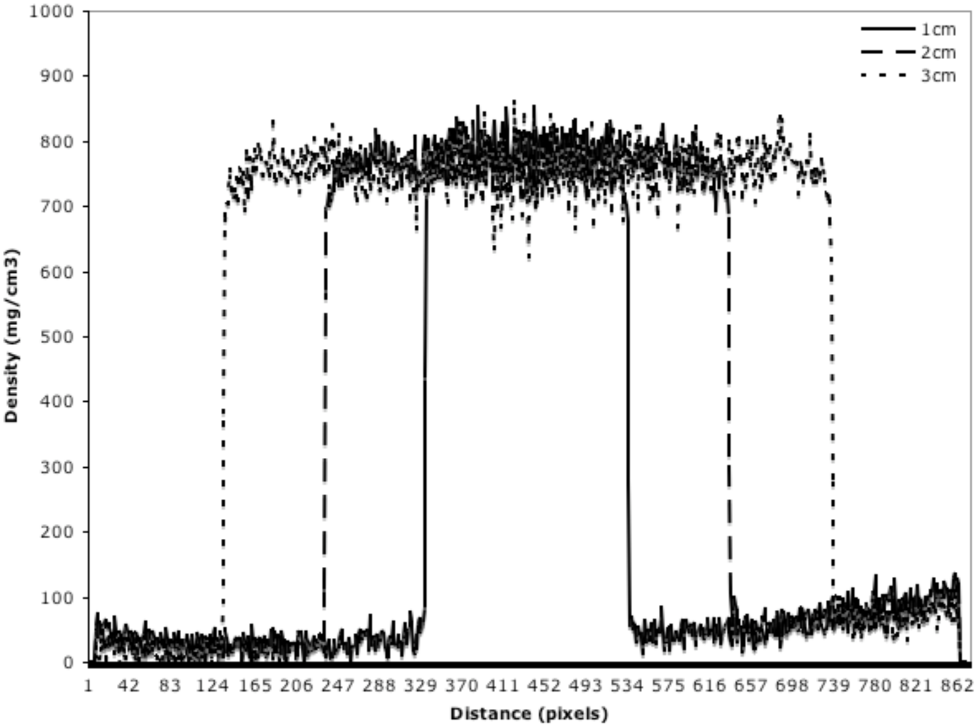

Figure 4.19: Profile plot across red line shown in Figure 4.18 (a-c) for corrected water phantom at 1, 2 & 3cm thickness.

4.2.4 Discussion

Although reconstructed images are by their nature artificial, practical steps can be taken to reduce inconsistencies and artifacts associated with micro-CT images within and across scanners. Such steps are paramount if any quantitative analysis is to be made with a degree of certainty.

The ball bearing phantom provided a simple tool for calculating the source-to-object and source-to-detector distance as a function of the gantry position. The example presented in Figure 4.13 clearly illustrates the difference between the original (a) and corrected (b) reconstruction image. Once determined, this calculated function can be implemented for all scan settings that maintain the same magnification. However, changes in the projection acquisition time will vary the acceleration and velocity path of the gantry between projections; this will introduce some additional variation. In general, it is best to determine the function for every unique scanning protocol and calculate the mean change over multiple phantom scans.

Using a similar approach to the dynamic source-to-object distance, a dynamic center offset as a function of the gantry position was also calculated using the ball bearing phantom scans. Implementation of this correction was also successful, although the improvement is not as dramatic as those seen in the dynamic source-to-center correction.

Ring artifacts are caused by insensitivities between adjacent detector elements. Using current detector technology, such insensitivities cannot be completely eliminated, but certain preventive / corrective approaches can be implemented to reduce their effects. Stabilization and maintenance of constant temperature during acquisition of projections was observed to be the best approach to reduce ring artifacts in the reconstructed images. Maintaining temperatures within a tight tolerance is quite difficult, especially in a large enclosure, such as the Siemens Micro-CAT-II where ring artifacts are still present. *In vivo* imaging becomes increasingly difficult as exposure times are kept to a minimum and the full dynamic range of the detector is not utilized, resulting in low signal to noise ratios. The ring artifact reduction algorithm described in this chapter provides a satisfactory reduction, and in the majority of cases where preventative steps have been adequately carried out, the final image has very minimal if any ring artifacts.

Beam hardening is a problem that cannot be avoided when utilizing a polychromatic X-ray source. When performing quantitative analysis of density and, in particular, regional difference in density, eliminating or reducing the effects of beam hardening is exceptionally important. The technique implemented and described in this chapter provided a simple means for correcting the effects of beam hardening for water. In the lung, air and water are the two primary components we are interested in; therefore, we focused on correcting the beam hardening for water. The corrected example, shown in Figure 4.18 and Figure 4.19, not only reduces the common cupping effect of beam hardening, but also reduces the difference in the density values of the same material over different thicknesses. Each X-ray energy protocol would thus require a unique set of polynomial coefficients, and with a predetermined workflow, calculation of these coefficients is a simple task.

With the exception of the ring artifact correction, the dynamic source-to-detector, center offset and beam hardening correction can be pre-determined once for any particular scan protocol. In such a situation, the time overhead is very minimal and results in a marked improvement to image resolution, quality and consistency. The ring artifact correction as currently implemented in Matlab (Mathworks, Natick MA) requires approximately two hours of processing per 2 GB dataset, however the algorithm is straightforward and would take no longer than five minutes if implemented in C++.

4.2.5 Conclusion

In this section, we have discussed several common artifacts and problems associated with reconstructed micro-CT images. With an understanding of the underlying mechanisms causing the described problems, we have implemented an array of practical solutions. The majority of the correction procedures detailed above can be performed once for each imaging protocol, with only the ring artifact correction requiring a unique computation for every dataset. The resultant data sets better represent the underlying object of interest and provide greater repeatability between scans.

4.3 *In Vivo Lung Imaging*

4.3.1 Introduction

The use of non-invasive imaging techniques can provide information for the progression of disease states and their response to therapies. Imaging mice poses new problems not seen in larger animals or in humans particularly because of their small size, and when performed *in vivo*, their rapid cardiac and respiratory rates also become an obstacle.

Micro-Computed Tomography (micro-CT) is an X-ray modality, which has become increasingly available as a solution to high-resolution non-invasive, fast through-put small animal imaging [39]. Maintaining a motionless state during scanning becomes increasingly difficult in live animal micro-CT imaging and can cause much of the resultant motion artifacts [155]. This is of even greater importance when studying the respiratory system, which contains important micro-structural pathology and anatomically expands and contracts with every breath. This combination of fine structure and constant macro-movement make this a very difficult organ to study *in vivo* using any imaging modality. Previously, it had been shown that respiratory and cardiac gating was possible for mice [156], although the power required from the X-ray source to capture each projection within a cardiac phase resulted in a X-ray resolution of approximately 100 microns due to the penumbra blurring and a final reconstructed image multiple orders worse. Numerous methods have also been proposed for reducing motion artifacts during acquisition of X-ray projections through timed exposure [155-159]. There have been simple, yet effective techniques which reduce the motion of the chest wall via physical sticky tape [160] in addition to recently advanced post-acquisition-gating techniques [161, 162]. All have shown an improvement over non-gating scans. However, no technique has been able to resolve lung structure below 150 microns *in vivo*. Until the time high-resolution projection images can be accurately acquired within a very short exposure time within the mouse respiratory and cardiac phase, there exists a great demand for a technique to image the respiratory system in the living mouse using current commercial micro-CT systems.

Our objective was to develop a reproducible technique for capturing the lung microstructure *in vivo* using high-resolution micro-CT. In this section, we present four different gating techniques, including a new computer controlled gating technique called the Intermittent Iso-pressure Breath Hold (IIBH), which induces a pseudo breath hold between hyperventilated cycles. The IIBH technique significantly reduces the motion artifacts, producing greater image resolution and contrast for respiratory research as compared to the three other methods.

Finally, qualitative and quantitative comparison between the techniques is presented through evaluation of several commonly applied lung imaging metrics.

4.3.2 Methods and Materials

4.3.2.1 Imtek Micro-CAT II Scanner

A Micro CAT II (Siemens Pre-Clinical, Knoxville, Tennessee) micro-computed tomography scanner was used throughout this study. This system was fitted with a Kevex (Thermo Electron Corp., Waltham, Massachusetts) micro-focus x-ray source capable of 0-500 μA and 0-130 kVp with a maximum total power output of 65 Watts. As the power increases the spot size will de-focus or bloom and an increase in penumbra blurring occurs. For example, at 60 kVp and a tube current of 500 μA the power level reaches 30watts resulting in a de-focused spot size of 42 microns. The detector consists of a phosphor screen connected via a fiber-optic taper to an intensified 3072x2048 pixel CCD containing a pixel pitch size of 32 microns. The distance between the X-ray source, detector and object can be altered via a manual gantry slide inside the scanner. Through custom configurations, various magnification levels can be achieved and hence different resolutions. To reduce beam hardening effects, a choice of different aluminum hardware filters was available; a 0.5mm Al filter was used for this study. For a field of view of 43x43mm, which is adequate for imaging an entire mouse lung of age 8-30 weeks, we determined the translated pixel size to be 14 microns (14 = 0.043/3072) at the detector for a binning of 1 or 28 microns (28 = 0.043/1536) for a binning of 2.

The scanner was set to 60 kVp, 500 μA, 500 ms camera exposure, binning of 2, 720 projections over 200 degrees (half-scan) with 100 bright and dark calibration images throughout this study. The total time for projection acquisition with no gating was 12 minutes, 15 minutes for respiratory-triggered imaging and approximately 35minutes for breath-hold gating. Projection slices are sent to a four node EXXIM Cobra (EXXIM Computing Corp., California) reconstruction server where 1024 slices are reconstructed using a modified Feldkamp algorithm [41], resulting in a voxel size of 28x28x28 microns. Total reconstruction time was 20 minutes. A total dosage of 84.5 Rad's (cGy) was estimated using the MicroCAT dosage calculator with the above settings and was equivalent throughout the gating techniques.

4.3.2.2 Scireq Flexivent Small Animal Ventilator

A Scireq Flexivent (Montreal, Quebec) small animal ventilator as shown in Figure 4.20 was used in this study. Several modifications were made to this unit to allow monitoring of respiratory phases for LabVIEW gating as well as interfacing a controlled air pressure system for the pseudo breath-hold. In particular, the expiratory solenoid was monitored and used as a trigger within the LabVIEW gating controller.

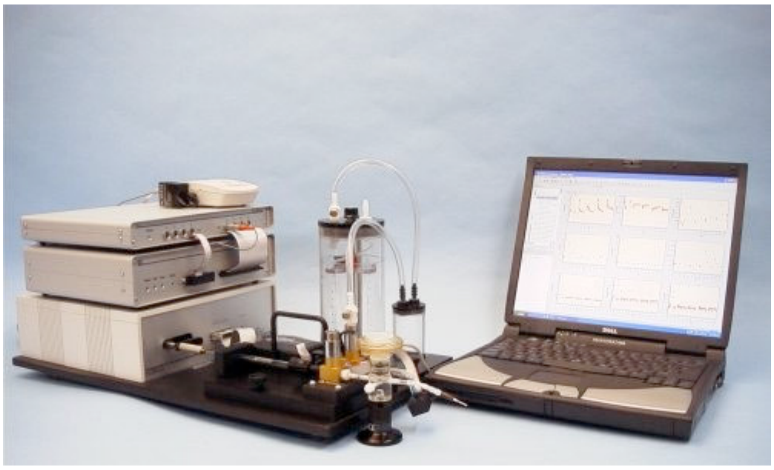

Figure 4.20: Scireq Flexivent small animal computer-controlled ventilator.

Almost any programmable ventilator could be used to implement the IIBH technique; the only requirement is the ability to start and stop the ventilator in a loop to allow the breath hold controller to activate the forced airway pressure.

4.3.2.3 Labview Gating Program

A custom LabVIEW (National Instruments, Austin, Texas) program was developed to trigger the micro-CT scanner through a transistor-transistor logic (TTL) signal depending on the different respiratory phases, which were monitored by a signal taken from the expiratory solenoid on the ventilator. A block diagram of this system is shown in Figure 4.21.

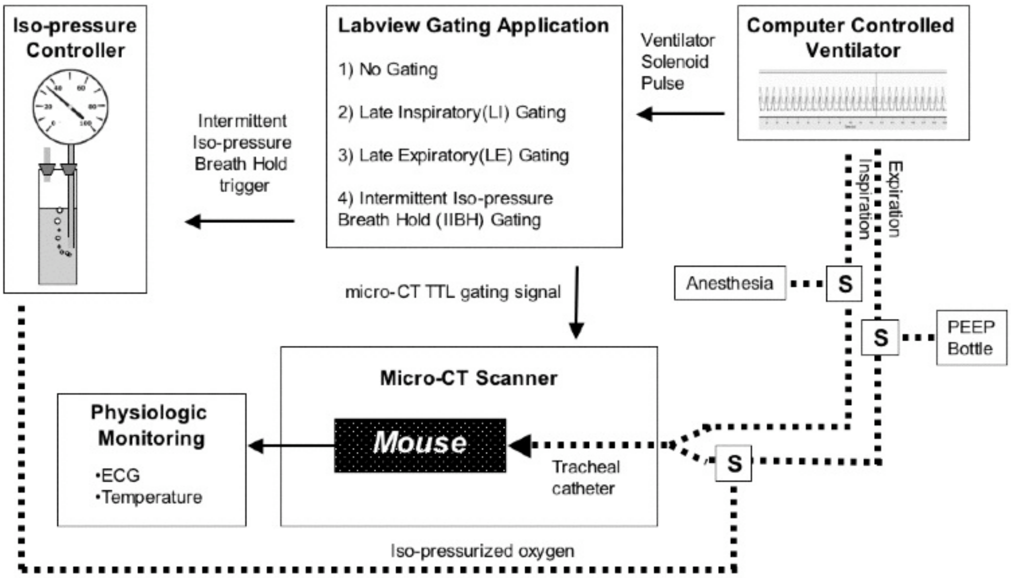

Figure 4.21. Respiratory Gating System Block Diagram. --- Dotted lines represent pneumatic pipeline. S - represents electronic controlled solenoids.

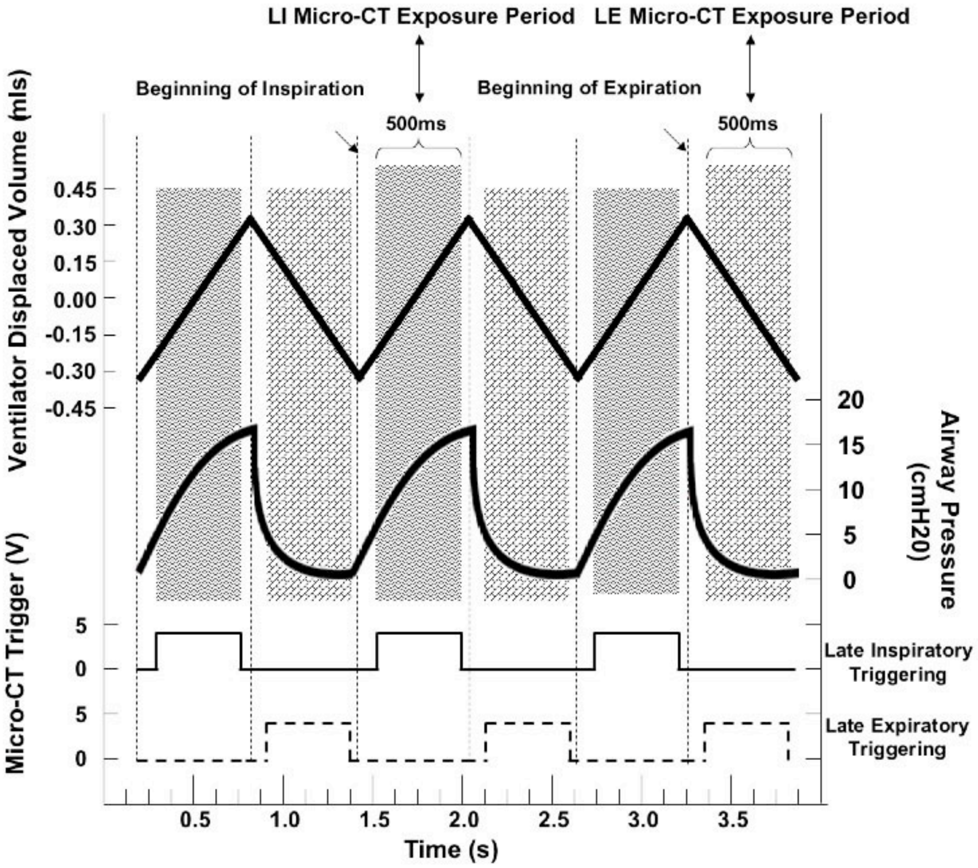

Figure 4.22. Late Inspiratory (solid) and Late Expiratory (dashed) gating waveform schematic.

Three gating techniques have been pre-defined: Late Expiratory (LE) triggering, Late Inspiratory (LI), and one new technique, which we have coined Intermittent Iso-pressure Breath Hold (IIBH) gating.

LE triggers 70ms post beginning of expiration at which time the 500ms exposure window is allowed to capture the lung through the majority of the expiration period as shown in Figure 4.22.

LI triggers 70ms post beginning of inspiration at which time the 500ms exposure window is allowed to capture the lung through the majority of the inspiration period as shown in Figure 4.22.

The 70ms delay from the beginning of each respiratory phase and triggering of the micro-CT scanner was chosen based on knowledge that there is less motion towards the end of each phase, thereby producing images with the least blurring.

The ventilator was set to 50breaths/min, a tidal volume of 35ml/kg and an I:E ratio of 1 for no gating, LE and LI gating. These settings were chosen to maintain a total minute ventilation of 1500-1800ml/kg/min between all gating techniques and were utilized for LE, LI and no gating in order to fit the micro-CT exposure window of 500ms within each 600ms inspiratory and expiratory phase.

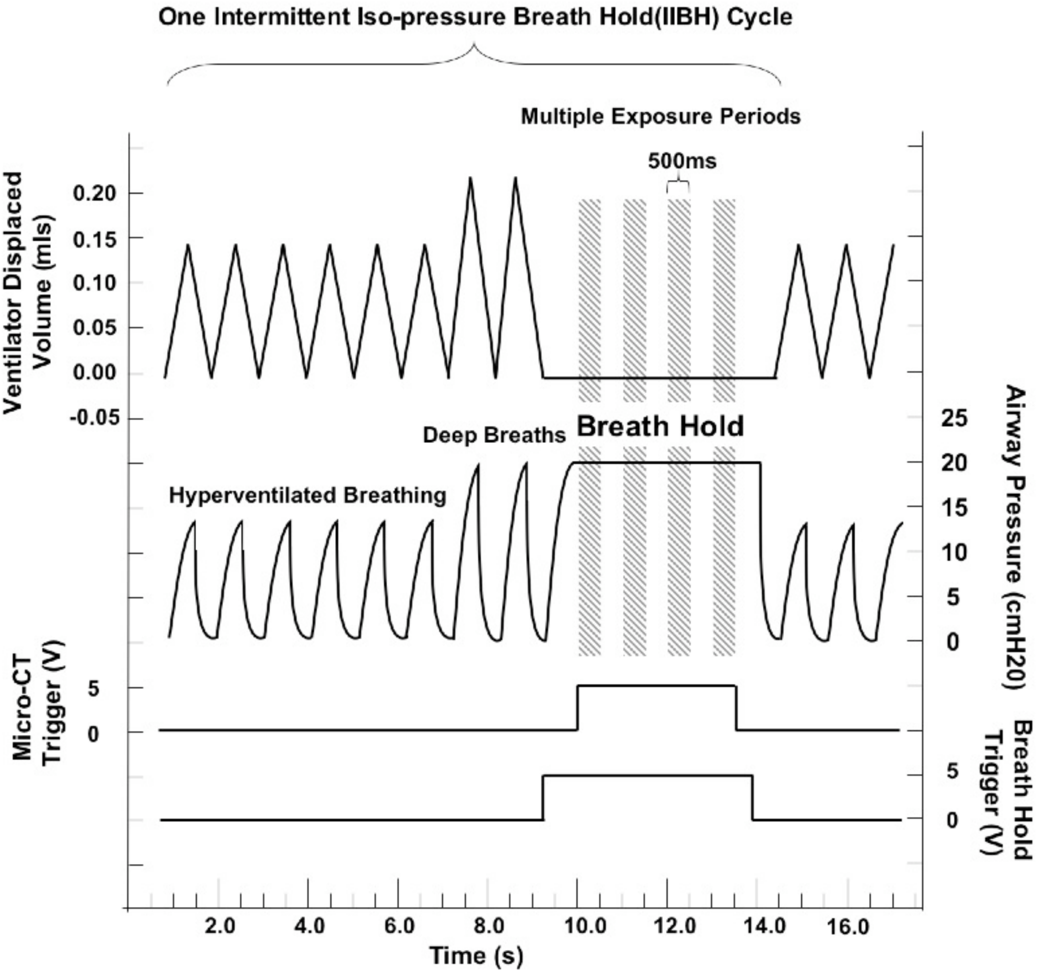

Figure 4.23: IIBH breathing sequence; hyperventilated breathing, two deep breaths (sighs) and no ventilation, triggering of a forced airway pressure (breath-hold), at which time the Micro-CT is triggered and multiple angles of view are acquired.

The new technique, IIBH gating, utilizes a special breathing pattern, which consists of three phases; 1) slightly hyperventilated breathing of 90br/min, 20ml/kg for 4-5 seconds, 2) two deep breaths followed by 3) apnea for a period of 5 seconds with a controlled forced air way pressure of 20 cmH_2O at which time the micro-CT scanner is triggered and allowed to capture several angles of view.

Figure 4.23 depicts this breathing cycle. The deep breaths prior to the breath-hold, ensure that the recruited volume inside the lungs are equivalent prior to each scan and reduces the possibility of atelectasis during acquisition.

4.3.2.4 Animal Preparation

Experimental procedures carried out in this study had been approved by the University of Iowa Animal Care Committee. Six normal male C57BL/6 mice aged 6-8 weeks, weighing between 20-25grams were used for this study. Each mouse was initially sedated using 3-4% isofluorane; the mice were then weighed and injected I.P. with 87.5mg/kg of ketamine and 12.5 mg/kg of xylazine. A tracheotomy was performed via a mid-line incision and insertion of a 20 gauge catheter; the open incision was then sutured as shown in Figure 4.24.

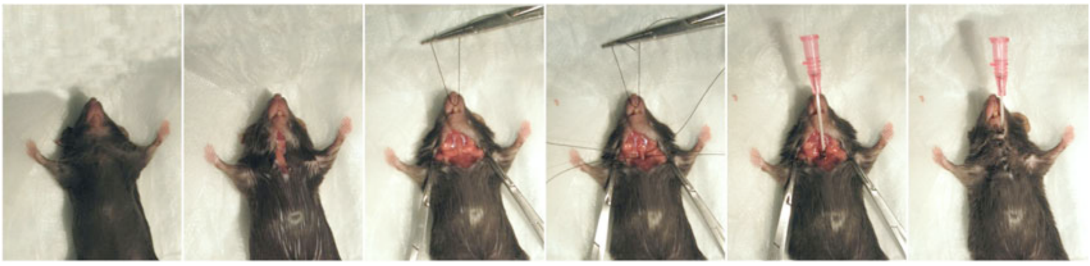

Figure 4.24: Mouse tracheotomy – surgical series from left to right.

The mouse was placed supine onto a polystyrene bed and mounted onto the Micro-CT carbon fiber animal stage. The polystyrene bed creates an ‘air’ equivalent border on the reconstructed images which allows for easier segmentation of the mouse body from the carbon fiber animal stage. ECG and temperature sensors were attached for physiologic monitoring using a BioVet C1 data acquisition system (Supertron Technologies, Newark, New Jersey). Respiratory paralysis was achieved by administering 0.1mg/kg of pancuronium I.P. at which time the tracheal catheter was connected to the Flexivent animal ventilator. The mouse was ventilated at 120br/min and tidal volume of 15ml/kg. Isofluorane was set to 3% initially and lowered to 1-2% once the heart rate was stable for maintenance of sedation throughout the imaging protocol.

Each of the six mice were scanned using the four gating techniques, one after another, followed by a randomly ordered repeat of the four scans, e.g. no gating, LE, LI, IIBH, LI, no gating, IIBH and finally LE. In total, eight scans were acquired for each mouse *in vivo*.

The first set of scans was used for qualitative and quantitative assessment, and the repeat was used to verify the repeatability of each technique.

Since we are presenting a non-survival pilot study in this section, a tracheotomy was carried out on all mice as opposed to intubation, which would otherwise allow for revival of mice. The techniques presented in this section have also been performed on intubated mice, which were subsequently revived, and are described in later chapters.

4.3.2.5 MTF Analysis

Determination of the Modular Transfer Function (MTF) for the scanner settings used throughout this study was performed using the following process. A 10-micron tungsten wire phantom (QRM, Nuremburg, Germany) was scanned on the Siemens Micro-CAT II at 60 kVp, 500 µA, 200 degrees, 720 Projections, 0.5 mm Al filter, reconstructed with a pixel size of 3.5 microns (8x over sampling). The intensity profile from an axial slice of the reconstructed tungsten wire phantom was extracted. The wire was modeled as a step function since its width is still too large to be considered as a point source. The DC components were removed and a Fast Fourier Transform was computed to result in Y(f) and X(f), where Y(f) is the FFT of the intensity profile and X(f) is the FFT of the step function. The MTF was then computed as MTF =Y(f) / X(f). The measurement of line pair per mm (1/f cutoff) was calculated at the 10% MTF point, and the final resolution is half of this period.

4.3.2.6 Diaphragm Density Profile

Four coronal slices from the same mouse using each gating technique were extracted from the dataset, and an intensity profile was calculated across the diaphragm. Anatomically, the lung-abdomen interface produces the greatest motion during breathing and is a representative position to measure lung motion. We calculate the slope representing the rate of change in the density between the interfaces for evaluation of the blurring. A greater slope represents a faster change, hence less blurring.

4.3.2.7 Airway Wall Density Profile

One area of interest for acquiring micro-CT images of mouse lungs is following airway wall thickening in diseased or challenged mice. In order to reliably make airway wall measurements in not only the central airways, but also in the small airways, minimization of motion artifacts is required.

A comparison of airway wall blurring artifacts has been conducted against each of the gating techniques. This was performed by calculating the slope at the wall to air interface inside the central airways.

4.3.2.8 Volume Repeatability

Lung volume measurement is an important anatomical descriptor that is often used in determination and progression of disease states. Validation of the accuracy and repeatability of measuring the mouse lung volume is an important and necessary step prior to biological studies. We performed digital volume analysis based on the repeated 3D micro-ct datasets from the six mice. Voxels within the chest cavity that exhibited Hounsfield Unit (HU) values less than -250 were accumulated and a final voxel count was used as the representative volume. This lung volume includes the parenchyma tissue, alveolar airspace and airways.

4.3.2.9 Air Content Repeatability Analysis

In all simplicity, the lung represents a large surface area over which gases are diffused in and out of the blood. Determination of ventilation and blood flow can themselves provide valuable information about the lung in its natural as well as diseased states. Air content analysis is a technique that provides information on the total percentage of air in any one region (voxel). CT images can be calibrated in CT numbers with Hounsfield Units (HU), which represent water as 0 and air as -1000 with partial volumes of each being represented on a linear scale from 0 to -1000. Air content can be extracted with relative ease from HU calibrated images acquired using the micro-CT. The air content was calculated by masking everything but the lung parenchyma for each axial slice and converting each voxel value using the following formula

$$\sum \frac{CT - CTair}{CTwater - CTair} \times 100 \ , \qquad 4.9$$

where CT is the CT number in HU at each voxel, CTair is the CT number value of air in HU as calculated from a region of the airway, CTwater is the CT number in HU of water as calculated from a central region of the heart. Voxels with an air content > 30% and < 95% are then accumulated and averaged for each axial slice [163]. The air content slope represents these average values for axial slices from the apex to the base of the lung. This was performed for each scanning technique and its repeat for each mouse.

4.3.3 Results

4.3.3.1 MTF analysis

The Modular Transfer Function (MTF) for the scanner settings used throughout this study was calculated. It was determined that the 10% MTF point is located at 9 lp/mm, which represents a resolution of 55 microns, and the 5% MTF point was located at 10.8 lp/mm, which represents a resolution of 46microns.

4.3.3.2 Subjective Comparison

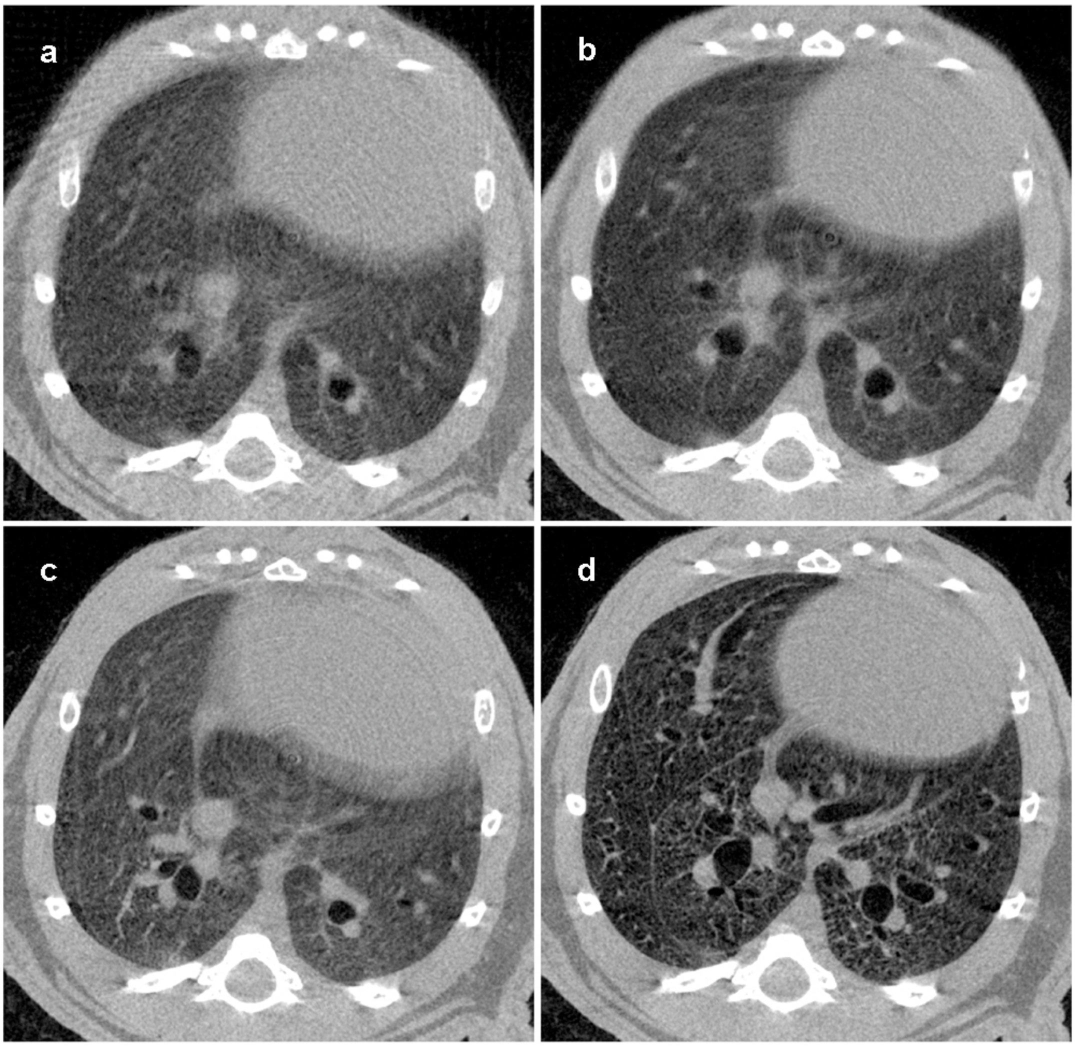

Figure 4.25. Axial slice gating comparison, a) No Gating, b) LI Gating, c) LE Gating, d) IIBH Gating. (window level -1000 to 2000 HU).

Figure 4.25 represents four axial slices from the same mouse using the four different gating techniques. A substantial difference is clearly apparent in Figure 4.25 between the gating modes. IIBH gating technique reduces and almost entirely eliminates respiratory motion artifacts. LE gating provides the best dynamic gating technique since there exists the least amount of motion during the later expiratory phase. No gating produced the worst images, since it inconsistently captures entire motion phases in random positions. No gating also produces streak artifacts, which are predominantly caused by the inconsistent position of the dense objects (ribs and spine) during acquisition. LI produced images better than no gating, but due to the large range of motion in the inspiratory phase, blurring is prominent. Also, in each image, motion artifacts due to the heart can be seen since there was no form of cardiac gating. Cardiac artifacts could be reduced through implementation of cardiac gating, requiring either multiple short exposures within a cardiac phase, or a higher power X-ray source as has been shown in [156]. However, multiple exposure acquisition on the current system would increase total imaging time ten fold, and the use of high-powered X-ray sources increases the penumbra blurring and hence reduces the final resolution. In all cases, the X-ray source and detector settings were identical and therefore dosage given to the animal was the same.

4.3.3.3 Diaphragm Density Profile

Figure 4.26 represents four coronal images from the same mouse using the four different gating techniques.

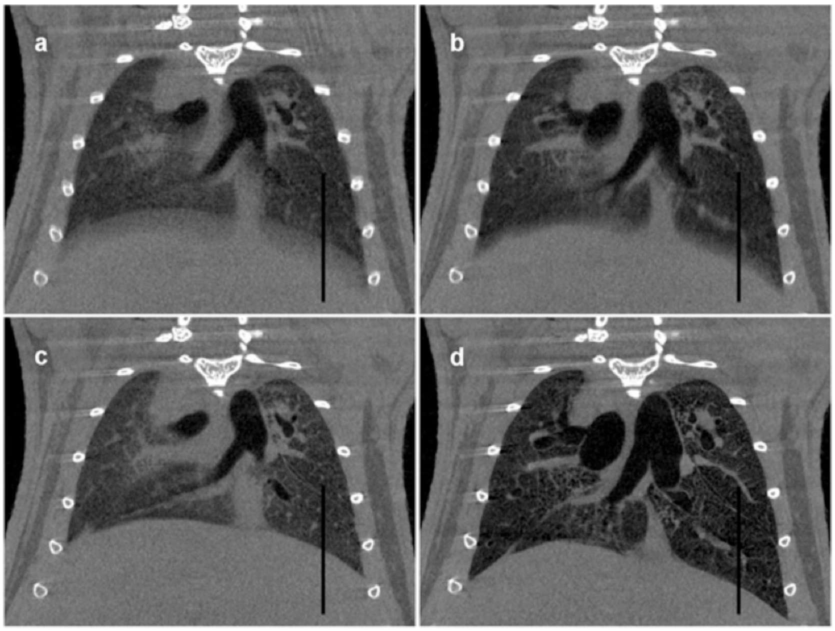

Figure 4.26: Coronal density profile, a) No Gating, b) LI Gating, c) LE Gating, d) IIBH Gating.

Figure 4.27 represents the intensity profile for the dark black lines found in Figure 4.26 across the diaphragm from top to bottom. The greater the slope represents a faster transition between lung-to-abdominal tissues, hence less blurring. As seen in Table 1, the IIBH gating produces a substantially larger slope with no gating producing the lowest value.

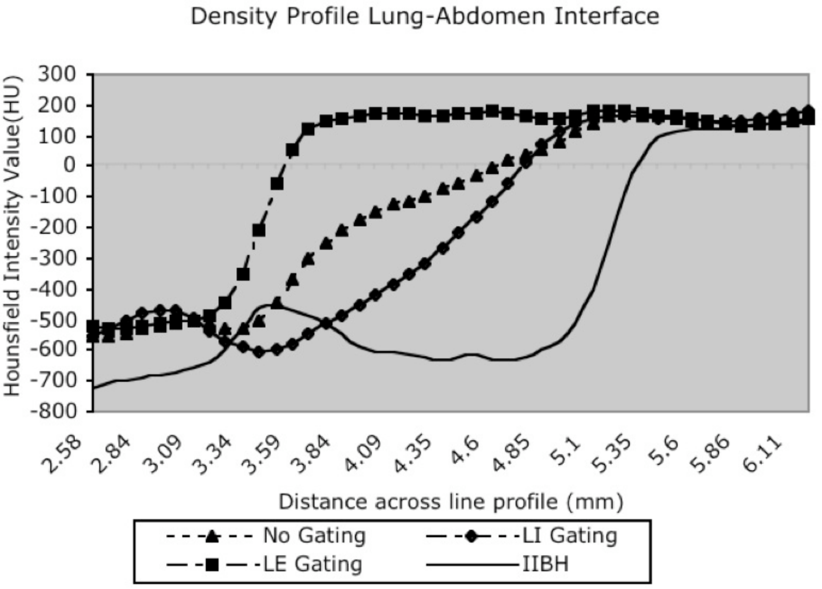

Figure 4.27: Density Profile of Lung-Abdomen Interface.

	Scanning Mode			
	No Gating	LI Gating	LE Gating	IIBH Gating
Slope HU/mm	375	490	1585	1924

Table 1. Density profile slope comparison.

4.3.3.4 Airway Wall Density Profile

Figure 4.28 represents the left and right main bronchus for the same mouse using the different gating techniques. Subjectively, we can see that the IIBH technique produces the clearest distinction between the air and wall interface. Quantitatively, through intensity profile plots across the air-wall interface of the right main bronchus as shown in Figure 4.29 and from Table 2, we can see that the slope for the IIBH gating is five times greater than the slope for no gating.

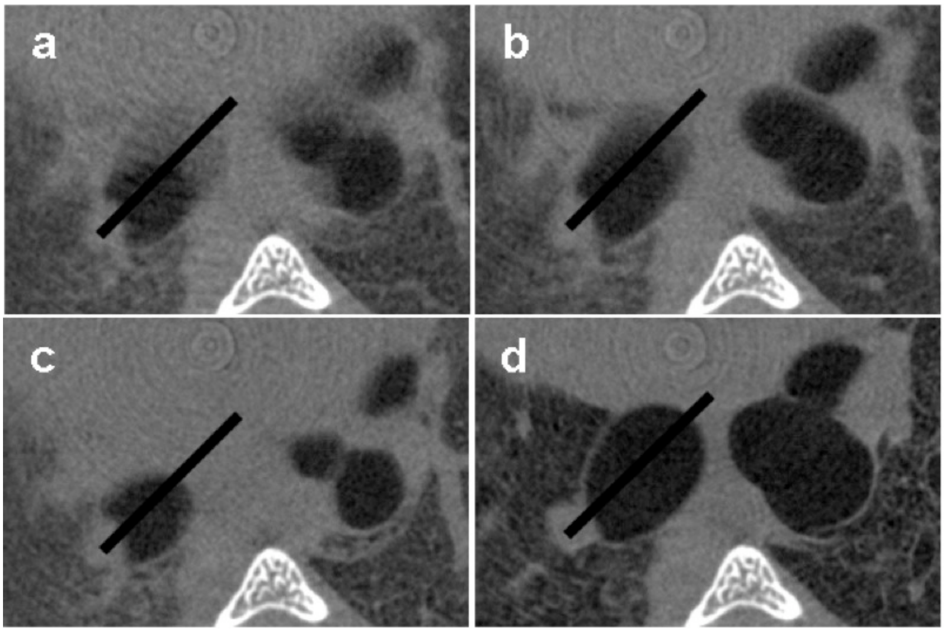

Figure 4.28: Right Main Bronchus Density Profile, a) No Gating, b) LI Gating, c) LE Gating, d) IIBH Gating.

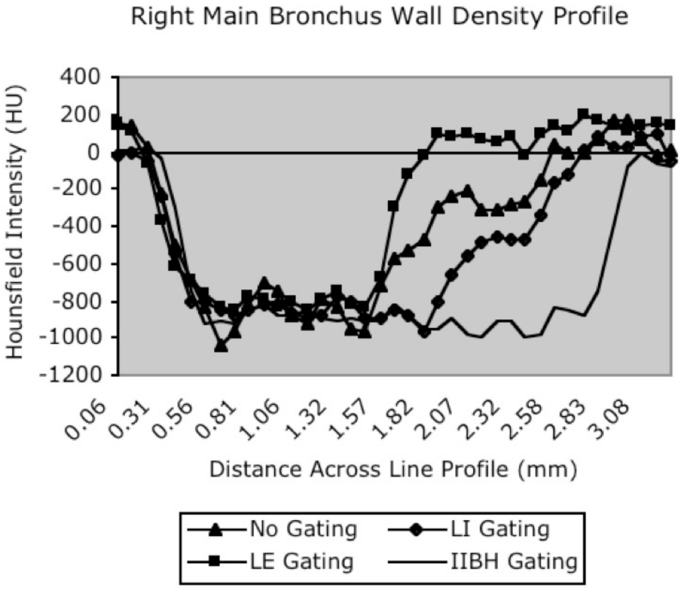

Figure 4.29: Right main bronchus density profile plot.

	Scanning Mode			
	No Gating	LI Gating	LE Gating	IIBH Gating
Slope HU/mm	774	1084	2610	4305

Table 2. Right Main Bronchus Density profile slope comparison.

4.3.3.5 Volume Repeatability

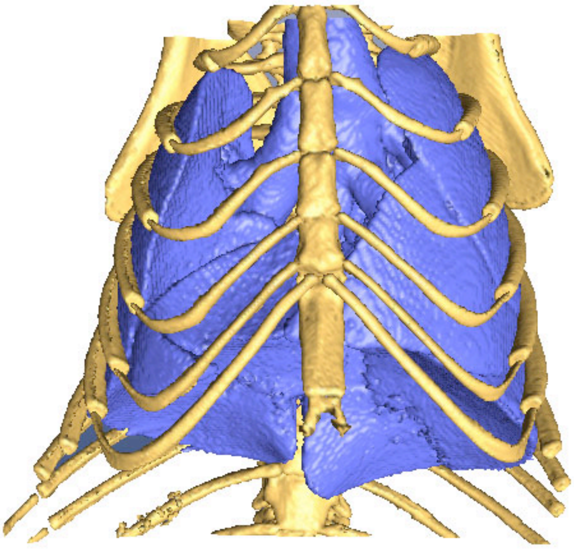

Figure 4.30: 3D reconstruction of the mouse lung and spine. Note the clear delineation of the ribs as well as lobar fissures and diaphragmatic surface indicating very accurate gating during scanning of a live breathing mouse.

Figure 4.30 represents a 3D reconstruction of a mouse lung surface with surrounding bone acquired using the IIBH gating. Here, we can see the accurate gating routine with clear delineation of the lobar fissures and diaphragmatic surface.

The volume for each mouse lung pair using the four different imaging techniques and their repeats were calculated. Figure 4.31 (a)-(d) represents Bland-Altman comparison graphs for trial 1 vs. trial 2 volumes for each of the mice for each imaging protocol, respectively. As seen by Figure 4.31 (d) the IIBH technique provides the greatest repeatability as determined by the smaller two standard deviations as shown by the dotted lines in the Bland-Altman graphs.

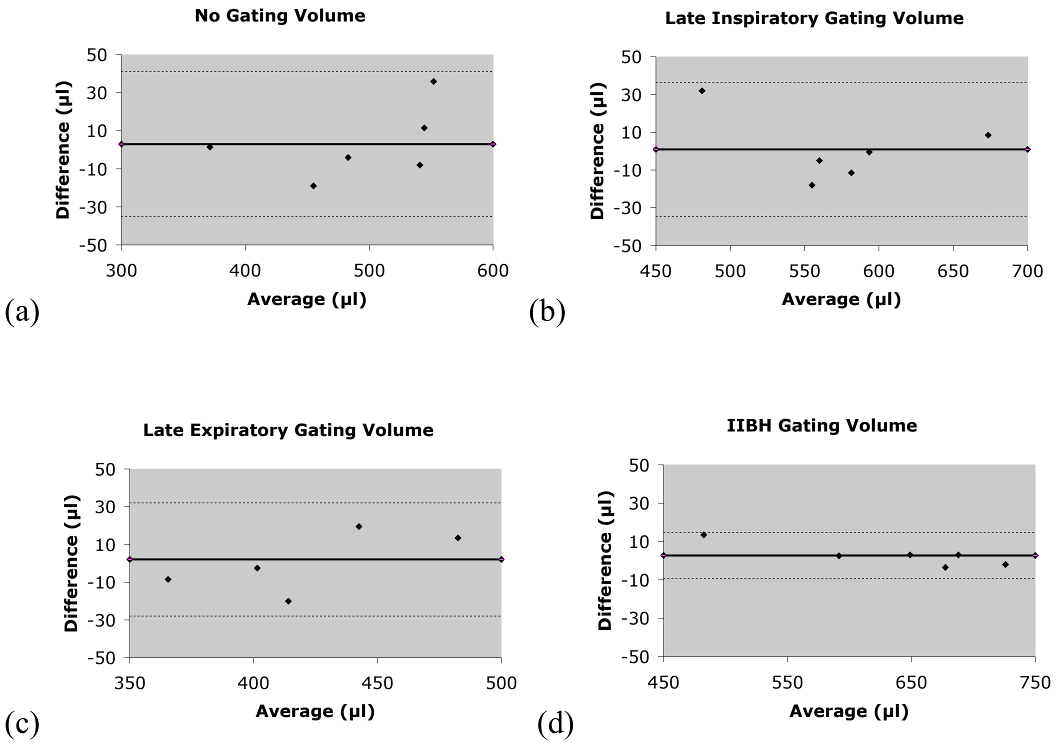

(a) (b) (c) (d)

Figure 4.31: (a) No gating, (b) LI gating, (c) LE gating, (d) IIBH gating volume repeatability curve (centerline represents mean, dotted lines represent two standard deviations).

4.3.3.6 Air Content Repeatability Analysis

Air content analysis was performed on each of the six mice. Figure 4.32 represents a Bland-Altman comparison graph for the air content slope for trial 1 vs. trial 2 for each mouse. Each point represents data from one mouse using the two repeat scans for the specific scanning technique. As seen in Figure 4.32, the IIBH technique provides the greatest repeatability as determined by the smaller two standard deviations as shown by the dotted lines in the Bland-Altman graphs.

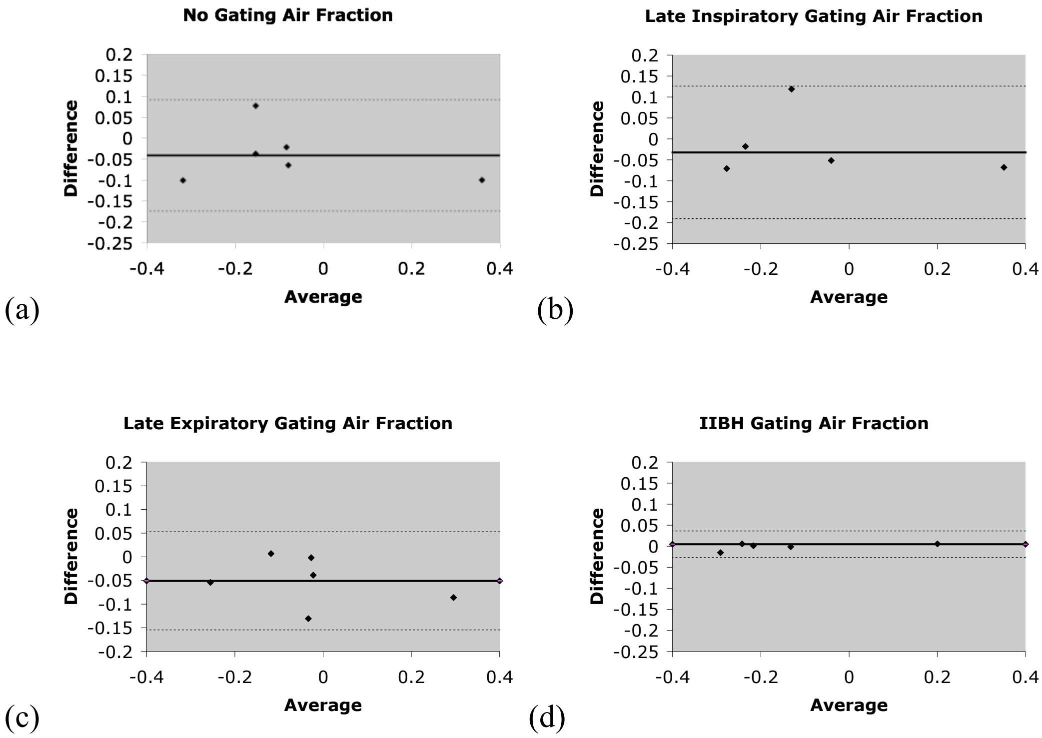

Figure 4.32: (a) No Gating, (b) LI Gating, (c) LE Gating, (d) IIBH Gating Air Content repeatability curve (centerline represents mean, dotted lines represent two standard deviations).

Figure 4.33 (a) represents an axial slice from the mid thoracic region of an IIBH scan where the mouse was placed supine, we can see the very slight increase in air content from the dependant to non-dependant region. Figure 4.33 (b) represents a coronal slice from the same mouse, here a slight increase in air content can be seen from apex to base. The change in air content for larger animals is more apparent, since it is thought to be due to the effects of gravity; hence the change is very small in mice lungs and may in fact be negligible when taking into consideration the density limitations of the scanner, something that requires further investigation.

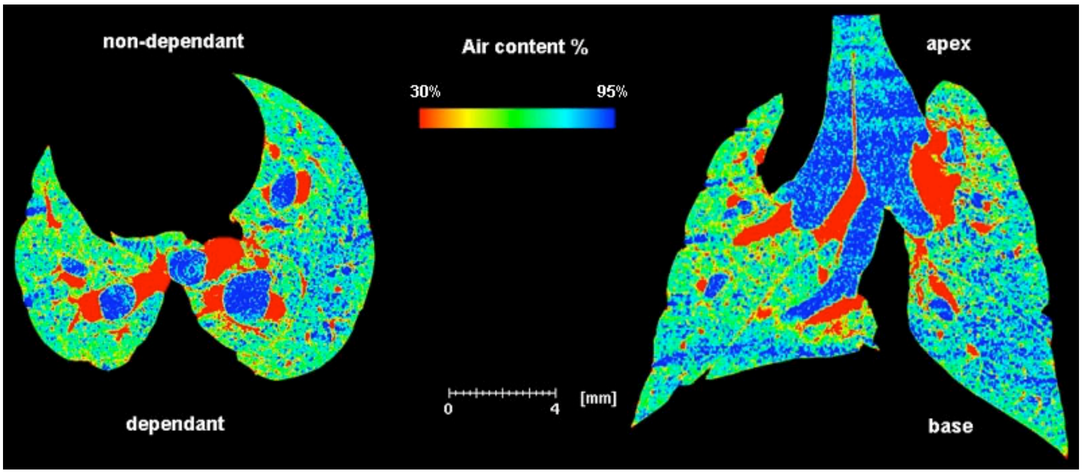

Figure 4.33.: a) axial & b) coronal 2D air content of mouse lung with air content color map. As seen in both, the change in air content is very slight, shifting from dependant to non-dependant in the axial and apex to the base in the coronal.

Figure 4.34 (a) represents a 3D reconstruction of the air content of a C57BL/6 mouse using the IIBH technique. Each voxel is color-coded and the 3D image has a transparency (alpha = 0.15) applied for greater visibility of voxels within the volume. In Figure 4.34 (b), we note the streaks seen at the top of the lung airways as denoted by the red arrows. These streaks are suspected to be the result of beam hardening predominantly caused by the spine and rib as seen by the superimposed 3D reconstruction of the bone structure. This artifact is less prominent in the distal lung regions, which could be accounted for by the chest wall and outer lung parenchyma having reduced the effect of the beam hardening. This is an important observation since the calibration of air inside the lung is commonly calculated at the trachea or at the right and left main bronchus carina. However, as seen here, these regions contain the greatest beam hardening artifacts for mouse lung scans, and the calculation of the air content should be made below this area. Also, it is worth noting that such large variations in density need to be accounted for if voxel density values are to be used quantitatively at a regional level.

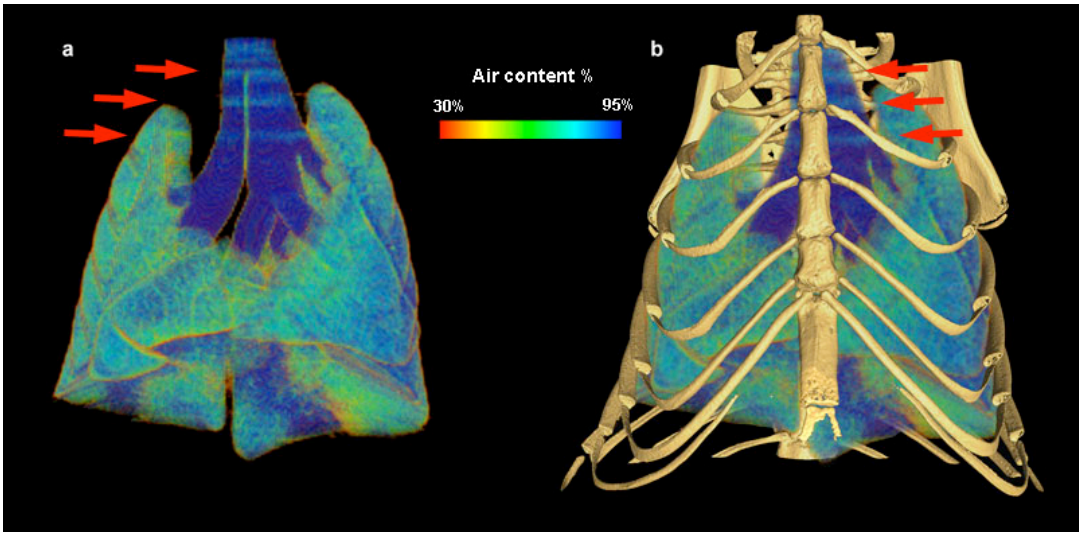

Figure 4.34.: a) 3D reconstruction of mouse lung air content with air content color map. b) same as (a) including spine and ribs, red arrows indicate beam hardening effects from the spine and ribs.

4.3.4 Discussion

The use of micro-CT imaging for the study of *in vivo* mouse pulmonary structure and function has been relatively limited by the low resolution, long scanning time and intrinsic motion artifacts. With the increasing availability of micro-CT scanners, there is a growing interest in using these systems for lung imaging; it has been shown that micro-CT imaging of mouse lungs is a source of valuable anatomic [156, 161, 164-166] and physiologic [157, 159, 160, 167] information for normal, and for acute and chronic diseased mice.

In this section, we have presented a new respiratory gating technique termed Intermittent Iso-pressure Breath Hold (IIBH), which reduces if not eliminates respiratory motion when acquiring projection images on a micro-CT system. This in turn reduces motion artifacts on the reconstructed images and increases the effective in plane resolution. The IIBH technique has been qualitatively and quantitatively assessed against three standard respiratory imaging techniques and has also been assessed for its repeatability in determining volume and air content. In all cases, the IIBH technique presented has been shown to be superior to currently used methods.

Using conventional ventilator settings with a smaller tidal volume would produce better results for the diaphragm and airway wall density profile for the no gating, LI and LE techniques. However, we were limited in maintaining the same exposure period (500ms) as well as total minute ventilation for all of the techniques, hence a slow breathing rate was chosen. In any event, from previous studies performed by other groups [155-158], it is clearly evident that all of these techniques produce images with resolution in the order of 2-3 times less, than those acquired using the IIBH technique.

Forcing a breath-hold on a normally free-breathing animal, does pose the question of possible adverse effects. Through our experience for normal mice, the settings presented have worked exceptionally well, and mice have been revived time over time as presented in a subsequent chapter, with no observed side effects. However, in diseased models such as emphysema, we increase the ventilation period incrementally as the disease progresses, and reduce the IIBH period to fit fewer exposure periods as a compensation to reduce the possible stress on the cardiovascular system of the mouse. By monitoring the mouse vitals, particularly the heart rate and $etCO_2$ if available, one can customize the settings for each mouse strain and disease state.

From previous studies [168] we know that a dosage of 100 cGy (taken as the standard dose for a Micro-CT scan) would represent 5% of the dose that kills 50% of mice within 30 days of exposure (LD 50/30). Also in an earlier study [169], Mole suggested mice could neutralize daily whole body doses of 25-50 cGy per day; he also noted that partial body irradiation reduced the recovery period. In our study, we determined the dosage for each scan with or without respiratory gating is on the order of ~85cGy. From this information we can conclude that although dosage is a critical element in developing imaging protocols using the micro-CT system and could ultimately limit the resolution, the potential for utilizing this system for longitudinal studies is viable.

4.3.5 Conclusions

The IIBH gating technique, presented in this section incorporates a constant pressure through out the airways, mimicking a human 'breath hold'. This approach ensures an almost motion-free lung during the acquisition period, without compromising the mice vitality. The IIBH method was found to be a superior technique when compared and analyzed against three other standard techniques in a qualitative, quantitative and repeatable setting. As seen in later chapters, using the presented gating technique further establishes the viability of longitudinal micro-CT respiratory studies.